



HAL
open science

Contributions of Ni-content and irradiation temperature to the kinetic of solute cluster formation and consequences on the hardening of VVER materials

C. Courilleau, Bertrand Radiguet, R. Chaouadi, E. Stergar, A. Duplessi,
Philippe Pareige

► To cite this version:

C. Courilleau, Bertrand Radiguet, R. Chaouadi, E. Stergar, A. Duplessi, et al.. Contributions of Ni-content and irradiation temperature to the kinetic of solute cluster formation and consequences on the hardening of VVER materials. *Journal of Nuclear Materials*, 2023, 585, pp.154616. 10.1016/j.jnucmat.2023.154616 . hal-04334904

HAL Id: hal-04334904

<https://normandie-univ.hal.science/hal-04334904>

Submitted on 12 Dec 2023

HAL is a multi-disciplinary open access archive for the deposit and dissemination of scientific research documents, whether they are published or not. The documents may come from teaching and research institutions in France or abroad, or from public or private research centers.

L'archive ouverte pluridisciplinaire **HAL**, est destinée au dépôt et à la diffusion de documents scientifiques de niveau recherche, publiés ou non, émanant des établissements d'enseignement et de recherche français ou étrangers, des laboratoires publics ou privés.

Contributions of Ni-content and irradiation temperature to the kinetic of solute cluster formation and consequences on the hardening of VVER materials

C. Courilleau^{a,b}, B. Radiguet^{a,*}, R. Chaouadi^b, E. Stergar^b, A. Duplessi^{a,b}, P. Pareige^a

^a Univ Rouen Normandie, CNRS, INSA Rouen Normandie, Groupe de Physique des Matériaux UMR 6634, F-76000 Rouen, France

^b SCK CEN, Boeretang 200, 2400 Mol, Belgium

ARTICLE INFO

Keywords:

Atom probe tomography

RPV steel

Neutron irradiation

Irradiation hardening

Solute cluster

ABSTRACT

The study of solute clusters induced by neutron irradiation is fundamental to the understanding of the embrittlement phenomena of Reactor Pressure Vessel (RPV) steels. In this paper, the influence of Ni-content and irradiation temperature on these cluster formation are investigated using atom probe tomography.

VVER 1000-BM (base metal) and 1000-W (weld) steels were chosen for their high Ni content of 1.2 and 1.7 at %, respectively. They were irradiated up to doses of 0.28 dpa at two temperatures (265 and 300 °C). The irradiations were performed at SCK CEN in the BR2 reactor.

After irradiation, Mn, Ni and Si rich clusters were observed. A careful study of their composition indicates that these clusters actually contain iron. Moreover, the evolution of Fe cluster concentration with the dose indicates a constant supply of solutes throughout the irradiation thanks to the flux coupling. With increasing dose, both the cluster size and number density increase.

The effect of temperature has to be dissociated from that of Ni content. Both of them result in an increase of the cluster number density at a given dose. The irradiation temperature has a more pronounced effect than chemical composition (mainly Ni effect). This can be explained by the fact that more matrix damage is produced at lower irradiation temperature. The influence of Ni on cluster number density is significantly higher at the lower temperature. All these observations support the hypothesis of radiation-induced segregation, even if a thermodynamic contribution to solute clustering cannot be excluded, in particular in the higher Ni steel irradiated at low temperature.

In all cases, the yield strength increases proportionally to the volume fraction of radiation-induced defects ($\sqrt{\langle V_D \rangle}$).

1. Introduction

Under operating conditions of a nuclear reactor, the reactor pressure vessel (RPV) steel undergoes a neutron flux that results in the formation of solute clusters. These clusters hinder the dislocation gliding, resulting in a hardening and embrittlement of the material [1–3].

Neutron irradiation produces an excess of point defects (PDs) – self-interstitial atoms (SIA) and vacancies [4] – that reach a steady state in term of concentration due to the balance between creation, recombination and loss to point defect sinks. These point defects enhance the atom diffusion. They also continuously diffuse towards sinks resulting in solute transport thanks to solute-SIA or solute-vacancy pair depending of

the solute nature [5]. These two mechanisms can result in radiation enhanced precipitation, as for Cu precipitates in RPV steels [6], and in radiation induced segregation or precipitation.

Mn-Ni-Si rich particles (MNSPs) are considered by several authors as thermodynamically stable phases at irradiation temperature resulting from radiation enhanced precipitation (REP) [7–9]. Modified Rietveld refinements of small Angle X-ray scattering analysis of RPV model samples irradiated at very high fluence [7] suggest that MNSPs has a G-phase crystallography. These MNSPs are also called “late blooming phases” because they grow very slowly after nucleation and are thus not detected at low dose [10]. On the other hand, different authors suggest that these features result from radiation-induced segregation (RIS) or

* Corresponding author.

E-mail address: bertrand.radiguet@univ-rouen.fr (B. Radiguet).

Table 1

Bulk compositions of VVER 1000-W and 1000-BM materials in at% and wt% [20]. Balance is Fe.

	Designation		C	Cr	Mn	Ni	Si	Cu	P	S	Mo	V
1000-BM	15Kh2NMFAA	at%	0.79	2.34	0.46	1.19	0.59	0.044	0.014	0.017	0.29	0.11
		wt%	0.17	2.20	0.46	1.26	0.30	0.05	0.008	0.010	0.50	0.10
1000-W	12Kh2N2MAA	at%	0.51	2.03	0.74	1.61	0.28	0.053	0.011	0.014	0.32	0.01
		wt%	0.11	1.90	0.73	1.70	0.14	0.06	0.006	0.008	0.55	0.01

Table 2

Mechanical properties in the unirradiated condition.

	Orientation	σ_y (MPa)	σ_u (MPa)	ε_u (%)	ε_t (%)	RA (%)	Orientation	USE (J)	T_{41J} (°C)
1000-BM	L	604	707	7	20	78	L-T	192	-70
1000-W	T	531	619	6	18	74	T-L	143	-58

radiation enhanced precipitation (RIP) [11–13]. The main difference in this case is that, due to flux coupling, MNSPs can appear in undersaturated solid solution, and in the case of supersaturated alloy or steel, the kinetics of formation of these features and the stationary states can differ from the one expected from REP. Solute clustering in ion irradiated under-saturated FeMn and FeNi model alloys was observed in [14,15], demonstrating the contribution of flux coupling in Mn and Ni clustering in ferrite.

The composition and kinetics of formation of these clusters depend on the material composition [16,17] and irradiation conditions. Ni and to a lesser extent Mn bulk concentrations play a preponderant role [16]. The higher the Ni level in the material, the higher the number density of clusters. The temperature is also a matter of importance and several regimes can be identified [4,18]. It has been shown in [19] that solute clusters are formed only at 300 °C and not at 150 or 400 °C.

The aim of this paper is to understand how the irradiation hardening of VVER materials is affected by Ni-content and by irradiation temperature through the formation of solute clusters. Moreover, by distinguishing between the effect of Ni-content and the effect of irradiation temperature, the kinetic of solute clusters formation and their consequences on the hardening of two VVER materials will be investigated.

This paper is divided into three parts. First, the method and the materials will be presented, followed by the results of the Atom Probe tomography (APT) analysis. Finally, the contribution of the bulk composition and the irradiation temperature will be discussed in terms of composition of the clusters and the existing correlation between number density of solute clusters and the induced hardening.

2. Experimental methods

2.1. Materials

The materials investigated in this paper were used within the IAEA coordinated Research Project (CRP) to better quantify the Ni-contribution to irradiation embrittlement of VVER-1000 reactors [20]. Both base metal and weld were provided by the Kurchatov Institute for further investigations within a consortium of seven participants, one of them being Institute of Energy Joint Research center (IE-JRC) in Petten from which we received a few broken Charpy specimens.

The steels nominal compositions (in wt% and at%) are given in Table 1 and their mechanical properties in the unirradiated condition are given in Table 2.

The 1000 weld metal (1000-W) is considered to have a high Ni content (1.60 at%) while the 1000 base metal (1000-BM) contains a medium Ni content of about 1.2 at%. It has to be noticed that the steel compositions also differ in the levels of Mn and Si. The 1000-W (high nickel contains twice more manganese and half silicon in comparison to the 1000-BM). However, the two main elements that are known to affect irradiation embrittlement, Cu-content and P-content, in these two materials are close and will have no significant effect [21,22]. The other

Table 3

Irradiation conditions for the 1000-BM and 1000-W samples. dpa is displacements per atom. Neutron fluxes and fluences are for energies higher than 1 MeV.

Material	T_{irrad} (°C)	Sample	Dose rate (10^{-8} dpa.s $^{-1}$)	Dose (dpa)	Flux ($E > 1$ MeV) (10^{17} n.m $^{-2}$.s $^{-1}$)	Fluence ($E > 1$ MeV) (10^{23} n.m $^{-2}$)
1000-BM	265 ± 2	LF265	1.4 ± 0.01	0.03 ± 0.01	1.0 ± 0.3	2.4 ± 0.1
		MF265	4.4 ± 0.01	0.10 ± 0.01	3.0 ± 0.4	7.3 ± 0.6
		HF265	11 ± 0.01	0.27 ± 0.01	7.7 ± 0.3	18.5 ± 0.4
	300 ± 2	LF300	1.6 ± 0.01	0.03 ± 0.01	1.1 ± 0.3	1.9 ± 0.4
		MF300	4.8 ± 0.01	0.08 ± 0.01	3.3 ± 0.4	5.8 ± 0.5
		HF300	12 ± 0.01	0.21 ± 0.01	8.4 ± 0.3	14.8 ± 0.3
1000-W	265 ± 2	LF265	2.0 ± 0.01	0.05 ± 0.01	1.4 ± 0.3	3.3 ± 0.1
		MF265	5.1 ± 0.01	0.12 ± 0.01	3.6 ± 0.4	8.5 ± 0.6
		HF265	12 ± 0.01	0.28 ± 0.01	8.1 ± 0.3	19.3 ± 0.4
	300 ± 2	LF300	2.2 ± 0.01	0.04 ± 0.01	1.5 ± 0.3	2.6 ± 0.4
		MF300	5.6 ± 0.01	0.10 ± 0.01	3.9 ± 0.4	6.8 ± 0.5
		HF300	13 ± 0.01	0.22 ± 0.01	8.8 ± 0.3	15.5 ± 0.3

elements, in particular Mn and Si, although often found in the irradiation-induced solute clusters have generally a weaker effect on the mechanical properties. So, it can be assumed that the difference observed between these two materials in terms of post irradiation behavior are largely due to the difference in Ni-content.

The tensile properties were derived from the tests performed at SCK CEN and the Charpy impact properties are those obtained at IE-JRC. It should be noticed that both materials exhibited significant variations in terms of Charpy impact properties of the VVER-1000-BM before irradiation, the T_{41J} -transition temperature varying between -103 and -49 °C while the upper shelf energy (USE) varies between 185 J and 270

Table 4

Results of the tensile tests, yield strength increase in MPa for the 1000-BM and 1000-W for each dose in dpa.

$T_{\text{irrad}} = 265\text{ }^{\circ}\text{C}$				$T_{\text{irrad}} = 300\text{ }^{\circ}\text{C}$			
Dose dpa	1000-BM	Dose (dpa)	1000-W	Dose (dpa)	1000-BM	Dose (dpa)	1000-W
	$\Delta\sigma_y$ (MPa)		$\Delta\sigma_y$ (MPa)		$\Delta\sigma_y$ (MPa)		$\Delta\sigma_y$ (MPa)
0.03	67	0.05	118	0.03	28	0.04	55
0.10	137	0.12	311	0.08	96	0.10	127
0.27	307	0.28	512	0.21	167	0.22	276

J, respectively. The weld metal is less heterogeneous and exhibits a T_{41J} value between -62 and $-40\text{ }^{\circ}\text{C}$ with a USE varying between 127 J and 160 J, respectively. The broken Charpy specimens being provided by IE-JRC and all specimens extracted from a small region, it is expected that material variability will be negligible. The yield strength values are in excellent agreement with those reported by Miller et al. [23], 599 and 536 MPa for the base metal and weld, respectively.

2.2. Irradiation conditions

These materials were irradiated in the BR2 reactor of the SCK CEN in Belgium to four different neutron doses and at two irradiation temperatures, $265\text{ }^{\circ}\text{C}$ and $300\text{ }^{\circ}\text{C}$, respectively. The irradiation temperature is

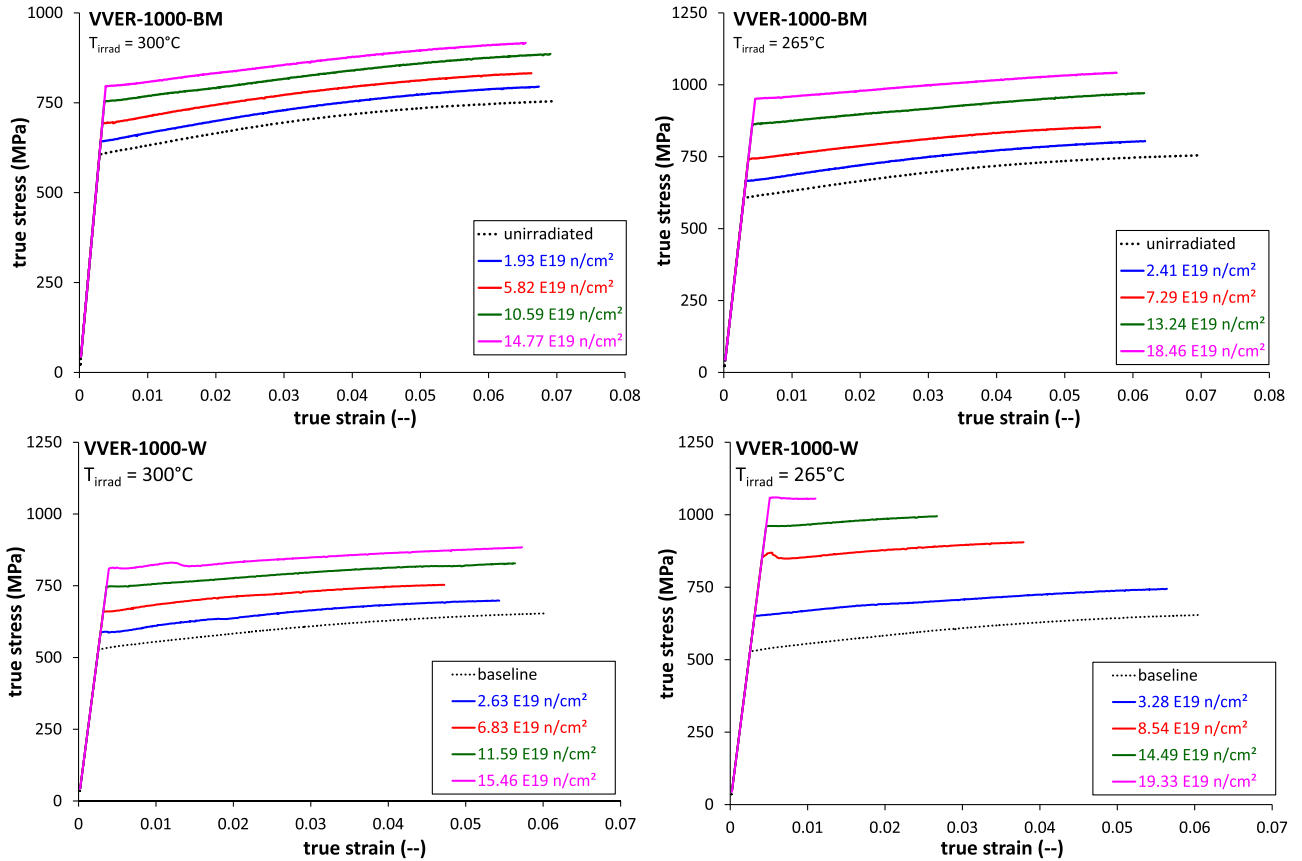


Fig. 1. Effect of irradiation on the true strain – true stress curves of the 1000-BM and 1000-W materials.

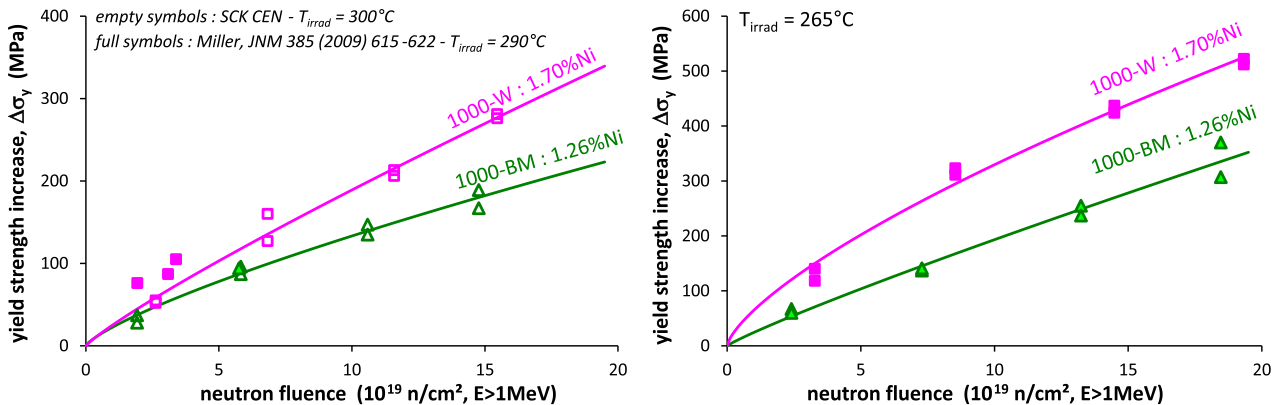


Fig. 2. Effect of irradiation on the yield strength increase in the 1000-BM and 1000-W materials.

Table 5

Matrix compositions of the unirradiated 1000-BM and 1000-W measured by APT and their bulk compositions for comparison. All concentrations are given in at%. The uncertainty corresponds to the standard deviation with a confidence interval of 95%. Fe is balance.

			C	Cr	Mn	Ni	Si	Cu	P	S	Mo	V
1000-BM	Matrix		0.11	1.50	0.35	1.23	0.63	0.01	0.01	–	0.21	0.03
		±	0.02	0.14	0.02	0.06	0.03	<0.01	<0.01	–	<0.01	0.02
1000-W	Bulk		0.78	2.34	0.46	1.19	0.59	0.04	0.01	0.02	0.29	0.11
	Matrix		0.16	1.61	0.63	1.68	0.50	0.06	0.01	–	0.28	0.00
		±	0.19	0.36	0.03	0.07	0.03	0.03	0.00	–	0.20	0.01
	Bulk		0.51	2.02	0.74	1.60	0.28	0.05	0.01	0.01	0.32	0.01

well controlled in the Callisto loop with a standard deviation of 0.7 °C of the pressurized water and an accuracy of less than ± 2 °C for the temperature of the specimens. Three levels of neutron doses were selected for investigation, LF, MF and HF designating low, medium and high fluence, respectively. The irradiation conditions are summarized in Table 3. It has to be noticed that BR2 is a material test reactor, thus neutron fluxes (10^{17} - 10^{18} $\text{m}^2\cdot\text{s}^{-1}$) are significantly higher than for VVER1000 reactor ($3\text{--}4 \times 10^{14}$ $\text{m}^2\cdot\text{s}^{-1}$) [24]. 2 to 3 order of magnitudes in the flux can result in differences in irradiation induced microstructures (it is generally admitted that higher flux result in smaller and more numerous solutes clusters but has limited impact on the mechanical properties [25]). Since the different fluences studied in this paper depend of the neutron flux, not of the irradiation duration, a flux effect could also be mixed with the fluence effects. However, the ratio between the lowest and highest fluxes are lower than 8 for the 1000-BM and lower than 6 for the 1000-W. These differences are low enough to consider that the flux effects should be small in comparison to fluence effect. This point is discussed later.

2.3. Tensile test

Cylindrical tensile specimens taken from broken Charpy specimens having a total length of 24 mm, a gage length of 12 mm and a cross section diameter of 2.4 mm were tested in a servohydraulic Instron machine under constant displacement rate of 0.2 mm/min. All tensile tests were performed at room temperature under a strain rate of 2.8×10^{-4} s^{-1} . Two out of the three available irradiated specimens were tested, the third specimen being kept as a spare in case of large discrepancies between the two tested specimens. The results in terms of irradiation-induced yield strength increase are reported in Table 4. In general, the yield strength measurement accuracy including experimental uncertainties and material variability is about ± 25 MPa.

The effect of irradiation on the stress-strain curve is shown in Fig. 1 for the two materials and irradiation conditions. Fig. 2 shown the effect of irradiation on hardening expressed as the yield strength increase. As it can be seen from Table 4 and Fig. 2, the range of yield strength increase is very large, varying between ~ 50 and ~ 500 MPa, which offers an

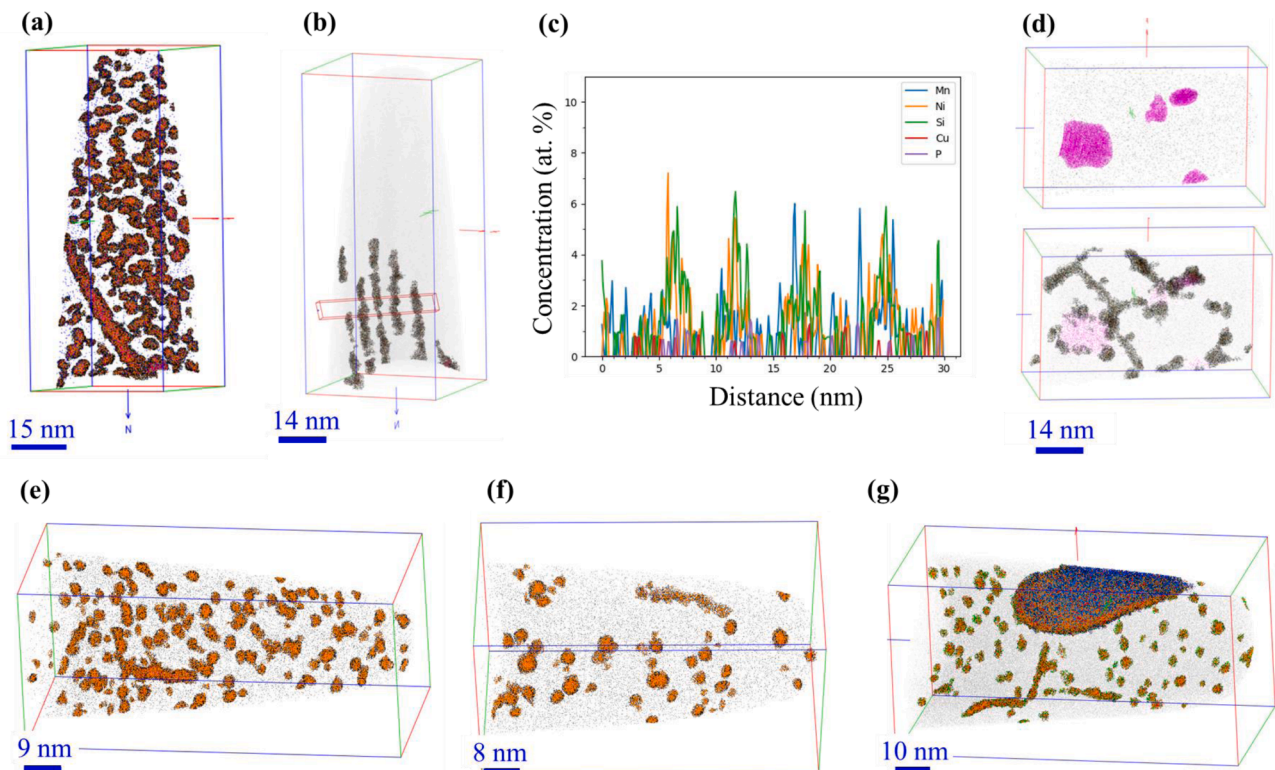


Fig. 3. Examples of observed microstructures in the irradiated in the samples irradiated at the highest fluences (a to d) 1000-W steel and (e, f) 1000-BM steel. (a) Region enriched in Mn, Ni and Si are highlighted using the Iso Position Method (IPM), showing solute clusters and segregation along dislocation lines after irradiation at 265 °C. (b) Segregation of Ni, Si and Mn along dislocations network of a low angle tilt boundary. The concentration profile shown in (c) is plotted along the red box. (d) Vanadium rich nitrides are shown in pink (upper image) and Mn, Ni and Si segregation along dislocation lines and on vanadium nitride interfaces are highlighted (bottom image) in 1000-W irradiated at 300 °C. In (e) and (f), region enriched in Mn, Ni and Si are highlighted using the Iso Position Method, showing solute clusters and segregation along dislocation lines after irradiation of the 1000 BM at high fluence at 265 °C and at 300 °C, respectively. In (g) Mn, Ni, Si rich clusters and segregations along dislocation lines and at carbide interface are highlighted in the 1000-BM irradiated at high fluence at 300 °C.

Table 6

Bulk and matrix concentrations in Ni, Mn, Si, Cu and P for the two materials in each condition, in at%. The compositions were measured with APT.

		Dose (dpa)		Bulk					Matrix				
				Ni	Mn	Si	Cu	P	Ni	Mn	Si	Cu	P
1000-BM	LF265	0.03		1.39	0.40	0.65	0.06	0.03	1.38	0.40	0.65	0.06	0.03
			±	0.03	<0.01	0.03	0.03	0.01	0.03	<0.01	0.03	0.03	<0.01
	MF265	0.10		1.34	0.37	0.68	0.08	0.02	1.28	0.36	0.64	0.06	0.02
			±	0.05	0.01	0.03	0.03	<0.01	0.06	0.01	0.03	0.01	<0.01
	HF265	0.27		1.26	0.35	0.65	0.04	0.01	0.95	0.30	0.47	0.03	0.01
			±	0.09	0.01	0.03	0.01	0.01	0.06	0.01	0.02	0.01	0.01
	LF300	0.03		1.29	0.37	0.66	0.04	0.01	1.29	0.37	0.66	0.04	0.01
			±	0.06	0.02	0.04	<0.01	0.01	0.06	0.02	0.04	<0.01	0.01
MF300	0.08		1.26	0.36	0.68	0.04	0.02	1.22	0.36	0.65	0.04	0.02	
		±	0.03	0.02	0.03	0.01	0.01	0.04	0.02	0.03	0.01	0.01	
HF300	0.21		1.30	0.37	0.68	0.05	0.01	1.16	0.36	0.59	0.04	0.01	
		±	0.08	0.02	0.02	<0.01	0.01	0.08	0.01	0.03	<0.01	0.01	
1000-W	LF265	0.05		1.61	0.61	0.50	0.05	0.01	1.56	0.59	0.48	0.05	0.01
			±	0.19	0.07	0.05	0.01	0.01	0.18	0.07	0.06	0.01	<0.01
	MF265	0.12		1.54	0.43	0.55	0.03	0.01	1.38	0.40	0.49	0.02	0.01
			±	0.05	0.06	0.03	0.01	<0.01	0.09	0.05	0.04	0.01	<0.01
	HF265	0.28		1.66	0.60	0.49	0.03	<0.01	0.97	0.40	0.20	0.02	0.01
			±	0.09	0.02	0.04	0.02	<0.01	0.21	0.06	0.11	0.02	0.01
	LF300	0.04		1.69	0.66	0.52	0.05	0.01	1.67	0.66	0.52	0.05	0.01
			±	0.10	0.03	0.03	0.01	0.01	0.07	0.02	0.02	0.01	0.01
MF300	0.10		1.65	0.64	0.49	0.05	0.02	1.55	0.62	0.45	0.05	0.01	
		±	0.12	0.10	0.06	0.01	0.01	0.07	0.09	0.04	<0.01	<0.01	
HF300	0.22		1.63	0.53	0.68	0.05	<0.01	1.49	0.50	0.62	0.04	<0.01	
		±	0.06	0.04	0.11	0.02	<0.01	0.09	0.02	0.14	0.02	<0.01	

interesting range to investigate the underlying microstructural changes.

2.4. Atom probe tomography

The materials for APT sample preparation were collected from the head of broken tensile bars. The APT tips were prepared using a FIB Scios Thermofisher Instrument to perform the lift-out step and a FIB ZEISS XB 540 for annular milling step. Two lamellas of each material were lifted-out in different locations of the sample to ensure the homogeneity of the material. For annular milling, the voltage was set to 30 keV and the current was varied from 700 to 50 pA. A final cleaning of 150 nm of the tip was performed with low energy Ga ions at 90 pA and 2 keV to remove the Ga implantation. At least three tips per material were analyzed.

The APT analyses were conducted on a LEAP 4000X HR from the GENESIS platform, before and after irradiation. All the analyses were carried out in voltage mode. A temperature of 60 K and a pulse fraction of 20% were found to provide the best compromise of settings to avoid early fracture of the specimen [26,27].

The IVAS software was used for 3D reconstructions. The field factor, k_f , was determined based on the measurement of the inter-reticular distance. Further data treatment was performed using the GPM 3D software. The solute clusters were identified using the isoposition method (IPM) [28]. First, thanks to a delocalization method, a local composition is attributed to the position of each atom, in particular the local concentration in Mn + Ni + Si, noted C_{MNP} . The distribution of C_{MNP} within the volume is calculated and compared to the distribution in the randomized volume (i.e. the atom positions are kept but their chemical natures are randomly swapped). The concentration threshold, C_{min} is given by the concentration corresponding to 0.01% of observation on the random distribution. All atoms for which $C_{MNP} > C_{min}$ are filtered. If the distance between 2 filtered atoms is smaller than $d_{max} = 0.4$ nm, they are considered to belong to the same cluster. In the analysis of the VVER materials, C_{min} is between 6 and 8%. To avoid the identification of statistical fluctuations as clusters, all clusters containing less than a minimum number of solute, N_{min} – for which no cluster is identified in the randomized volume – are not considered. This threshold N_{min} is between 6 and 12 atoms, depending on the analyzed volume. Once the clusters are identified, they are grouped into two to three

size classes depending on their number density (N_d). The radius is determined after an erosion treatment whose limit is set at the mid-height of the concentration profile of each size class. The radius given in this study is the radius calculated from the number of atoms in the cluster after this erosion step : $R = (3V_{at}N / 4\pi Q)^{1/3}$ where V_{at} is the atomic volume in α -Fe, N the number of atom in a cluster and Q the detection efficiency. Finally, the composition is extracted from the mass spectrum after a second erosion process whose limit is set to completely remove the interface and keep only the cluster core.

3. Results

3.1. Un-irradiated samples

First, the unirradiated materials were analyzed. As expected no MNS rich clusters were found in non-irradiated steels. Only ferritic matrix was analyzed in the 1000-BM whereas several Mn, Mo and Cr rich carbo-nitrides were detected in the 1000-W. Their composition (in at%) is Cr-(49.2 ± 1.0%), Mo-(11.8 ± 0.6%), Mn-(3.9 ± 0.4%), C-(17.5 ± 0.7%), N-(7.4 ± 0.5%), balance is Fe.

The matrix compositions of the two materials are reported in Table 5 and are found to be in good agreement with the bulk compositions except for carbon and carbide-former elements (Cr, Mn, Mo, V) which are depleted in the matrix.

3.2. Irradiated samples

As it is shown in the Fig. 3, different features were observed in irradiated samples. As in the un-irradiated materials, a carbide was observed in the 1000-BM irradiated in HF-300 condition. Its composition in at.% is Fe-(36.1 ± 0.1), Cr-(34.1 ± 0.1), Mo-(2.55 ± 0.04), Mn-(2.58 ± 0.04), C-(22.1 ± 0.1). The balance is the sum of other solute concentrations (about 2 at.% in total). In the 1000-W irradiated in the same conditions, plate shaped vanadium rich nitrides were observed in several 2 vol (both coming from the same sample area). Excluding Fe, the main elements in these features are V (13.2 at.%), Cr (6.2 at.%) and N (10.1 at.%). Carbides and nitrides were likely present in the material before irradiation. Concerning the irradiation induced features, Mn, Ni and Si rich clusters located in the matrix were observed in all conditions.

Table 7

Number density (N_d) and radius (R) of solute clusters for each irradiation condition in 1000 BM and 1000 W steels. Uncertainties are given by the standard deviations.

	T_{irrad} (°C)	Dose (dpa)	R (nm)	σ_R (nm)	N_d (10^{23} m^{-3})	σ_{N_d} (10^{23} m^{-3})
1000-W	265	0.05	1.04	± 0.02	12.4	± 4.9
		0.12	1.10	± 0.06	24.1	± 5.6
		0.28	1.20	± 0.14	40.9	± 2.3
	300	0.04	0.90	± 0.11	5.0	± 1.6
		0.10	1.02	± 0.15	6.5	± 3.5
		0.22	1.13	± 0.13	10.7	± 3.2
1000-BM	265	0.03	0.96	± 0.07	3.2	± 1.6
		0.10	1.02	± 0.08	11.7	± 3.0
		0.27	1.14	± 0.05	24.7	± 2.4
	300	0.03	0.91	± 0.18	2.0	± 1.8
		0.08	1.01	± 0.15	3.5	± 2.0
		0.21	1.11	± 0.11	8.1	± 1.9

Such clusters were also observed at the interface of the vanadium rich nitrides. Segregations of the same solutes were also observed along dislocation lines, at grain boundary and at all interfaces between carbide or V rich carbides and the ferritic matrix. A few amounts of Cu and or P is sometime associated to these cluster or segregations.

The Table 6 summarizes the global (including all observed features) and the matrix concentrations in Ni, Mn, Si, Cu and P of all investigated materials and irradiation conditions. The global concentrations in the irradiated samples are similar to the matrix ones in the non-irradiated condition. On the contrary, the irradiated matrix is depleted in Ni, Mn and Si at medium and high neutron exposure in both steels and irradiation temperatures. The matrix depletion in Ni, Mn and Si is maximal for the highest doses.

The evolution of the matrix composition is explained by the formation of Mn, Ni and Si rich clusters and continuous segregations along dislocation lines, at interfaces and grain boundaries.

Details about solute clusters as a function of material (so that, Ni content) and irradiation condition (temperature and dose) will be given in the next section.

3.2.1. Cluster size and number density

Numerous clusters were observed in 3D reconstructions, at all irradiation conditions. Their number density (N_d) and average radius (R) are summarized in Table 7. To avoid any bias due to the presence of V-rich nitrides, the volumes containing such features were not considered for the calculation of cluster characteristics.

The average cluster radius slightly increases with the dose but no significant differences between the materials are observed. On the other hand, the number density of clusters drastically increases with the dose. The number density is also significantly affected by the material composition and irradiation temperature. The highest N_d corresponds to

the highest irradiation dose (0.28 dpa), the lowest temperature (265 °C) and the 1000 W material which contains the highest Ni level.

3.2.2. Cluster composition

The clusters compositions in terms of Ni, Mn, Si, Cu and P (all enriched solutes in comparison to the matrix composition) and Fe for the two materials under the different irradiation conditions are reported in Table 8. The main solute in the clusters is the Ni, up to 17.9% for the 1000-W samples irradiated at 265 °C to the highest neutron dose, Mn-content is between 1.5 and 5.5%, Si-content between 3.5 and 9.8%. Fe is also detected in the clusters. Its concentration is rather high (65–80%) and decreases with the neutron fluence. The lowest Fe-content (around 65%) corresponds to the highest doses and the lowest irradiation temperature (265 °C).

Here, it should be mentioned that similar steels were also investigated by APT after neutron irradiation by Miller et al. [12,23]. Irradiation were performed at about 290 °C under lower flux and up to fluences comparable to the low and medium fluences studies here. There is a reasonably good agreement between the data published in [12] - cluster diameter, density and Fe level are respectively 2–4 nm, 1×10^{23} in BM to $1.5 \times 10^{23} \text{ m}^{-3}$ in WM and about 75at.% for a fluence comparable to our low fluence - and the results obtained in the present work. On the contrary, in [23] (fluences comparable to our low and medium ones), clusters observed both in the weld and the base metal are significantly smaller (~1 nm in diameter), more numerous and contain about 10% Fe only (it should be noted that there is the same discrepancy between [12,23] for the low fluence irradiation). The difference in size and number density between our results and [23] are the opposite to flux effect expectations. The differences in the number densities are hardly explainable. Concerning the size and the Fe level, the figure 7 in [23] shows an average radial concentration profile of 30 nanoclusters at the highest fluence in the BM. In this profile, it is clear that the total amount of solutes in the cluster core does not exceed 25 at.% (so that Fe level is about 75%). In addition, when the authors give the cluster composition (with only 10 at.%Fe), they mention that "the envelope algorithm is extremely aggressive in removing the matrix atoms. Therefore, the ratios of the elements provide a more reliable estimate of the concentrations rather than the absolute levels." From our point of view, the aggressive algorithm used by Miller et al. explain the underestimation of the measured Fe level and likely the smaller radius.

4. Discussion

Before discussing the detailed results in terms of composition and distribution of the irradiation-induced defects, it is important to point out for the following preliminary remarks.

First, the focus of this paper is on the effect of Ni-content although other chemical elements are different when comparing 1000-BM to 1000-W. The main purpose is not to quantitatively compare these two

Table 8

Chemical composition of the clusters. Concentrations are given in at.%. Balance is the constituted of the other solutes.

	T_{irrad} (°C)	dose (dpa)	Fe	Ni	Mn	Si	Cu	P
1000-W	265	0.05	76.2 ± 1.5	11.8 ± 0.4	3.9 ± 0.8	3.5 ± 0.9	0.71 ± 0.15	0.27 ± 0.16
		0.12	73.7 ± 1.7	15.0 ± 1.1	2.5 ± 0.7	5.6 ± 0.9	0.28 ± 0.11	0.15 ± 0.09
		0.28	64.7 ± 3.1	17.9 ± 1.5	5.5 ± 0.9	8.6 ± 1.9	0.22 ± 0.13	$0.130.13$
	300	0.04	72.9 ± 1.5	13.4 ± 3.2	3.9 ± 0.7	1.9 ± 2.9	0.63 ± 0.44	0.52 ± 0.35
		0.1	72.5 ± 4.6	13.9 ± 2.1	2.8 ± 0.8	6.2 ± 1.6	0.43 ± 0.24	0.82 ± 0.59
		0.22	67.7 ± 3.2	16.9 ± 1.0	2.5 ± 1.0	7.6 ± 2.5	0.39 ± 0.2	n.s.
1000-BM	265	0.03	79.8 ± 5.7	10.6 ± 0.6	1.9 ± 0.7	2.1 ± 2.2	0.14 ± 0.12	0.57 ± 0.40
		0.1	77.4 ± 1.5	10.5 ± 0.8	2.2 ± 0.3	5.2 ± 1.3	0.55 ± 0.16	0.26 ± 0.14
		0.27	73.5 ± 1.7	13.0 ± 1.1	2.6 ± 0.2	8.4 ± 1.3	0.38 ± 0.16	0.21 ± 0.09
	300	0.03	79.8 ± 5.7	10.4 ± 5.9	1.5 ± 2.2	0.9 ± 1.6	0.14 ± 0.14	0.88 ± 0.48
		0.08	70.9 ± 9.1	12.2 ± 2.1	1.5 ± 0.4	5.4 ± 10.3	0.29 ± 0.18	1.33 ± 0.91
		0.21	68.3 ± 4.3	15.5 ± 2.4	2.4 ± 1.44	9.8 ± 2.6	0.22 ± 0.14	0.36 ± 0.26

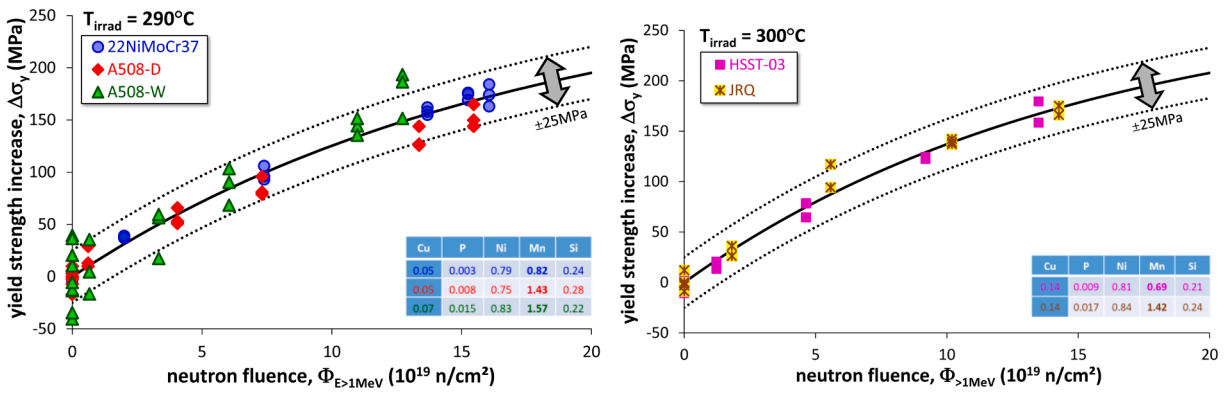


Fig. 4. Experimental data obtained on irradiated RPV materials irradiated in the BR2 MTR reactor exhibiting a negligible effect of Mn-content.

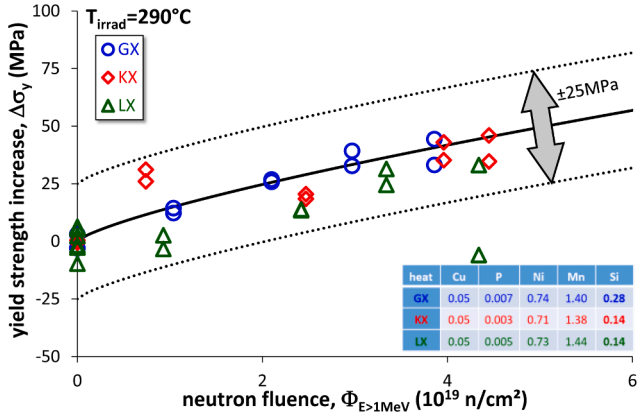


Fig. 5. Experimental data obtained on irradiated RPV materials irradiated in the BR2 MTR reactor exhibiting a negligible effect of Si-content.

materials with respect to Ni-content. However, the two materials clearly exhibit different Ni-contents, 1.26% versus 1.70% weight-% for 1000-BM and 1000-W, respectively, and therefore these values are significantly different to compare these materials with respect to post-irradiation behavior.

Second, the two other elements that are known to significantly affect irradiation behavior, Cu and P, are significantly low (0.05–0.06% for Cu and 0.006–0.008% for P) to produce a significant effect. Based on the analysis of large experimental databases using artificial neural networks that demonstrated that Cu, Ni and P elements dominate the post-irradiation embrittlement [21,22], the effects of all other elements is

assume to be weaker than Ni one. The fact that Mn and Si are found in the neutron-induced solute clusters do not necessarily mean that they have a large contribution into hardening and embrittlement. Available experimental data also support the negligible effect of Mn and Si. Fig. 4 shows some comparative test results obtained on materials irradiated in the same irradiation campaigns in the BR2 reactor with similar chemical composition except Mn-content. The same observation can be made on the minor effect of Si-content on irradiation hardening, as illustrated in Fig. 5 where doubling Si-content (from 0.14% to 0.28%) does clearly not affect the irradiation-induced hardening.

Of course, microstructural investigations should be necessary to confirm the weaker effect of Mn and Si on solute clustering. However, based on mechanical properties data, we will assume in this paper that the main differences observed in the microstructures of the two steels come from the Ni-content.

Finally, from the irradiation point of view, all specimens were irradiated during one BR2 cycle of three weeks, approximately 500 h. This means that the specimens were irradiated at different neutron fluxes, the higher the fluence, the higher the flux. However, the differences in terms of flux are still small, between 1×10^{13} and 8.6×10^{13} n/cm², $E > 1$ MeV. Such a difference is not expected to produce significant effects contrary to comparison between vessel flux conditions ($\sim 10^{10}$ – 10^{11} n/cm²s) and MTR irradiation conditions ($\sim 10^{13}$ n/cm²s) such as the BR2. This is also confirmed by the experimental data reported in [20] where the neutron flux was ranging between 0.03 and 3×10^{13} n/cm².s, $E > 1$ MeV. The results are shown in Fig. 6 where the available data obtained in different reactors, including research and power reactors are compiled. The experimental data reported in [20] were expressed in terms of T_{41J} as a function of neutron exposure for energy above 0.5 MeV. To be combined in a single plot, the following neutron energy ratio ($\phi_{E > 0.5 \text{ MeV}} / \phi_{E > 1 \text{ MeV}}$)

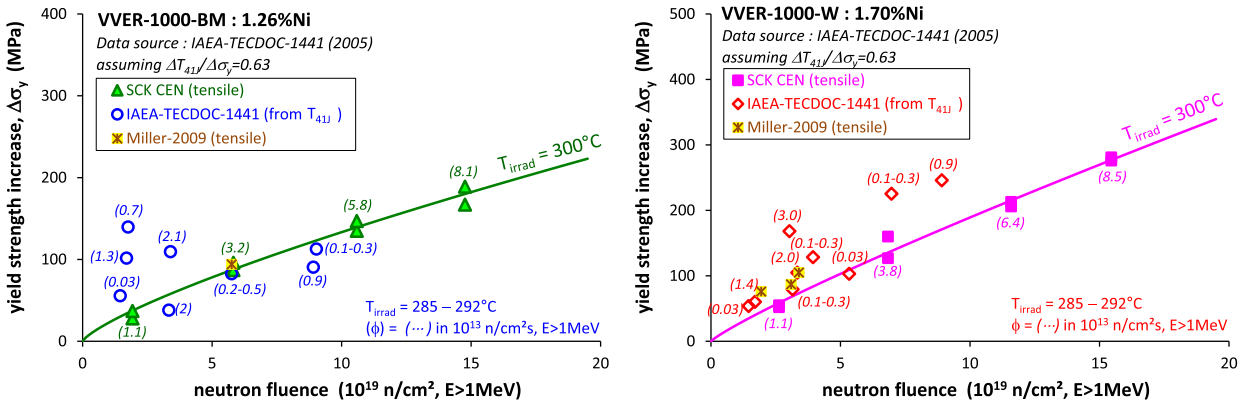


Fig. 6. Yield strength increase as a function of neutron exposure : comparison with irradiation-induced hardening extracted from the Charpy impact test data assuming an embrittlement-to-hardening ratio of 0.63.

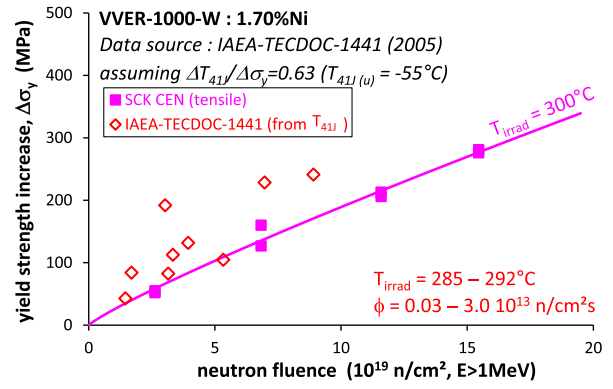
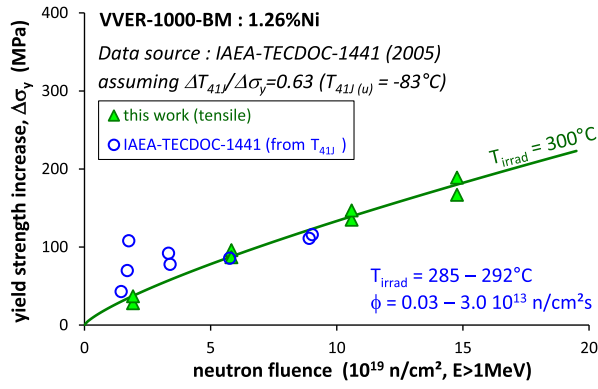


Fig. 7. Yield strength increase as a function of neutron exposure: comparison with irradiation-induced hardening extracted from the Charpy impact test data assuming an embrittlement-to-hardening ratio of 0.63 and a constant $T_{41J(u)}$ before irradiation.

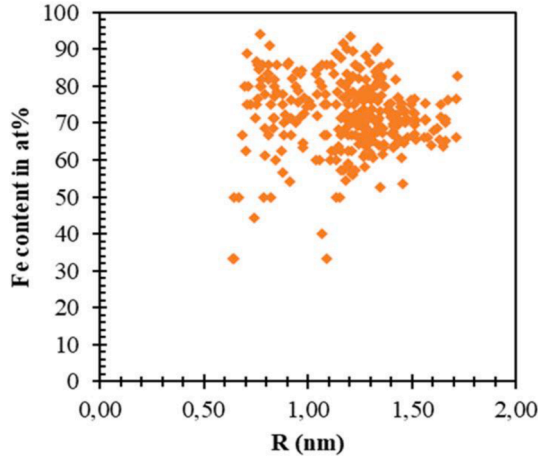


Fig. 8. Fe content measured in cluster cores as a function of cluster radius within one volume of the 1000-BM HF265. Each dot is a cluster. There were 390 clusters in the volume.

and embrittlement-to-hardening ratio ($\Delta T_{41J}/\Delta\sigma_y$) had to be applied for consistency:

$$\frac{\phi_{E>0.5MeV}}{\phi_{E>1MeV}} = 1.65 \quad (1)$$

and

$$\frac{\Delta T_{41J}}{\Delta\sigma_y} = 0.6^\circ\text{C} / \text{MPa}^3 \quad (2)$$

As it can be seen from Fig. 6, the comparison between the data derived from the Charpy impact data reported in [20] and the data of the present paper are in a reasonable agreement. It is also interesting to note that, as indicated earlier, the flux does not play a significant role, Fig. 6 showing no obvious trend with respect to flux. Note that if unique unirradiated properties are considered rather than individually measured by the various organizations, the scatter is slightly reduced but still present (see Fig. 7) with no evidence of flux effect.

By analyzing the materials irradiated in the present work and irradiated in the BR2 reactor, many uncertainties and biases that can originate from different irradiation conditions, different fluence and dosimetry evaluations, different materials locations, and different testing conditions will be minimized. In other words, the experimental and testing variables that can bias our observations are reduced to a minimum, namely, Ni-content, irradiation temperature and neutron fluence. The remaining variables such as neutron flux and other

elements than Ni-content can be neglected.

4.1. Cluster composition

4.1.1. Fe in the clusters

Fig. 8 shows the Fe-content measured in the clusters core as a function of cluster radius within one volume of the 1000-BM HF265 specimen. No evolution of Fe-concentration with the size is observed. Such high amount of iron in the cluster cores was measured in all irradiation conditions, in both steels. The presence of a majority of iron detected in the solute clusters formed under irradiation in RPV steels is a common observation [26,27]. However, several authors consider that the Fe is not part of the cluster but is only a probe artefact [29–31] (and in some cases, the measured level of iron is simply not reported). Indeed, it is well known that – due to a modification of the local radius of curvature – trajectory aberrations can occur when the evaporation field of a chemical heterogeneity differs from the one of the surrounding matrix [32,33]. In the case of a low evaporation field chemical heterogeneity (as the irradiation-induced solute clusters in RPV steels), ion trajectories are focused resulting locally in a higher local atom density than expected. If the difference of evaporation fields is high enough, trajectory overlaps can occur and artificially introduce matrix atoms in the cluster [34]. However, modeling of field evaporation of APT needles containing low field clusters has shown that for a difference of evaporation field between cluster and matrix lower than 15% (which is the case here, considering evaporation fields of Fe 33 V/nm, Ni 35 V/nm, Mn 30 V/nm and Si 35 V/nm), trajectory overlap do not modify significantly the core composition of clusters larger than 1 nm in diameter [33,35].

More recently, Hatzoglou et al. [36,37] proposed an analytical model to estimate the proportion of matrix atoms that are introduced in the cluster core by using the particle density and a shape factor according to Eq. (1).

$$C_{cor} = C_{meas} \cdot \rho \cdot S + C_{mat} \cdot (1 - \rho \cdot S) \quad (1)$$

where ρ is the reduced density, $S = XY/Z^2$ the shape factor, X, Y and Z are the particle lengths along the 3 directions. C_{cor} , C_{meas} and C_{mat} are the corrected concentration, the measured one in the cluster core and in the matrix, respectively. This model was applied to nano-oxides in ODS steels [36] and to α' precipitates in the FeCr system [38], showing that the iron detected in the cluster core can be an artefact (case of ODS steel) or can be actually there (case of α' precipitates).

Here, the correction was applied to several clusters – 10 clusters coming from 3 different tips – and the Fe-content is found to be about $72.5 \pm 3.0\%$, which is in good agreement with the concentration measured from the mass spectrum of cluster cores ($72.8 \pm 2.2\%$). In the light of these results, the Fe found in the clusters cannot be entirely considered as an atom probe artefact but as is part of the clusters. Thus

Table 9

Chemical composition of the clusters. Concentrations are given in at.%. Balance is the constituted of the other solutes. Error bars are given by 2 standard deviations.

	T_{irrad} (°C)	dose (dpa)	Ni	Si	Mn
1000-W	265	0.05	61.5 ± 0.4	18.2 ± 0.3	20.3 ± 0.4
		0.12	64.9 ± 0.2	24.2 ± 0.2	10.8 ± 0.1
		0.28	55.9 ± 0.2	26.9 ± 0.2	17.2 ± 0.2
300	300	0.04	69.8 ± 1.0	9.9 ± 0.6	20.3 ± 0.8
		0.1	60.7 ± 0.5	27.1 ± 0.4	12.2 ± 0.3
		0.22	62.6 ± 0.4	28.1 ± 0.3	9.3 ± 0.2
1000-BM	265	0.03	72.6 ± 1.1	14.4 ± 0.9	13.0 ± 0.9
		0.1	58.7 ± 0.3	29.1 ± 0.3	12.3 ± 0.2
		0.27	54.2 ± 0.2	35.0 ± 0.2	10.8 ± 0.1
	300	0.03	81.3 ± 1.0	7.0 ± 0.7	11.7 ± 0.8
		0.08	63.9 ± 1.3	28.3 ± 1.2	7.9 ± 0.7
		0.21	56.0 ± 0.6	35.4 ± 0.5	8.7 ± 0.3

the cluster composition strongly differ from G-phase: $(\text{Ni}, \text{Fe}, \text{Mo})_{55\%}$, $\text{Si}_{24\%}$, $(\text{Mn}, \text{Cr})_{21\%}$; or Γ_2 -phase : $\text{Ni}_{50\%}$, $\text{Si}_{16.7\%}$, $\text{Mn}_{33.3\%}$.

4.1.2. Composition of the clusters and segregation on dislocations

In order to confirm previous conclusion, the composition of the clusters considering only Ni, Si and Mn is reported in the Table 9. Excepted for the Weld metal irradiated at the highest fluence that could correspond to G-phase (removing iron without any objective reason), any composition corresponds to G- or Γ_2 -phases.

Fig. 9(a) shows the relative proportion of solutes in the clusters as a function of their concentration in the bulk for all investigated conditions in terms of material, dose and irradiation temperature. Fig. 9(b) shows the same plot but for segregations along dislocation lines. These graphs highlight the existing link between the material composition and the solute segregation. This correlation had already been formulated given that the composition of segregation depends on the material composition [16,17]. Since both clusters and dislocations are enriched in the same way, it strongly suggests that the same formation mechanism is involved.

4.2. Dose effect on size, number density and cluster composition

The cluster number density, N_d and average radius, R , increase with neutron dose, as shown in Fig. 10(a) and b), regardless of composition or irradiation temperature. Considering that the clusters are not

precipitates of a well-defined phase as discussed previously, their formation mechanism can be related to an induced segregation mechanism – thanks to the flux coupling – on small point defect clusters [39,40]. Recently, Castin et al. [41] have shown that the efficiency of this mechanism based on Object Kinetic Monte Carlo simulations highlighted the role of immobilized self-interstitial loops in the first stage of formation of solute clusters.

The experimental observations shown here are coherent with this mechanism, the continuous increase in solute cluster number density with dose results from the increase in defect sink density as irradiation continuously produces new point defects. The increase in size and solute content, relative to Fe-content (Fig. 10c) and d)) of the clusters with neutron dose can be explained by the flux of point defect that continuously bring solutes to sinks during irradiation.

4.3. Ni concentration and irradiation temperature contributions

As it was said previously, the two steel compositions differ not only from Ni level but also from Mn and Si concentrations (considering solute taking part of the clusters). Based on the fact that the effect of Mn and Si on mechanical properties is low in comparison to Ni effect, as explained before, we assume here that the main effect of the composition is Ni effect.

The cluster characteristic which differs the most from one material or one temperature to another one is the number density, N_d . To distinguish the effect of chemical composition from the effect of irradiation temperature, the ratio of N_d was calculated for each pair of parameters. However, before deriving such ratios, an interpolation procedure should be applied to normalize the N_d values to the same reference dose. Three reference doses were selected, 0.05 dpa, 0.09 dpa and 0.22 dpa, respectively.

Fig. 11 shows the contribution of each parameter, i.e. the Ni-content and the irradiation temperature. The error bars are calculated from the N_d uncertainties. For example, $N_{d265}/N_{d300(W)}$ is the N_d of 1000-W at 265 °C divided by the N_d of 1000-W at 300 °C, this ratio quantifies the contribution of irradiation temperature. The open symbols represent the effect of temperature, and more specifically, the orange circle is for the 1000-W and the green square is for the 1000-BM. The black triangles and the blue diamonds represent the effect of composition at 265 °C and at 300 °C, respectively.

At low and medium neutron doses, the difference between the ratios is difficult to assess due to the magnitude of the uncertainty. However,

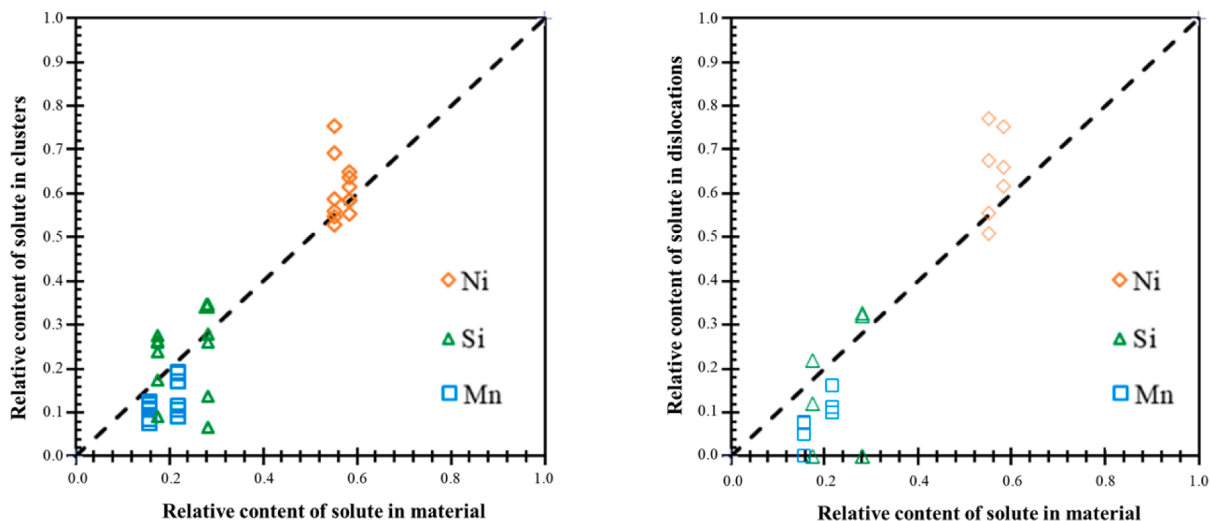


Fig. 9. Relative proportion of segregated/clustered solutes against their proportion in the unirradiated material for all materials and conditions. e.g. relative proportion of Ni = $C_{\text{Ni}} / (C_{\text{Ni}} + C_{\text{Mn}} + C_{\text{Si}})$. (a) solute clusters and (b) segregations along dislocation lines. The Cu and P were not considered because their concentrations are rather small.

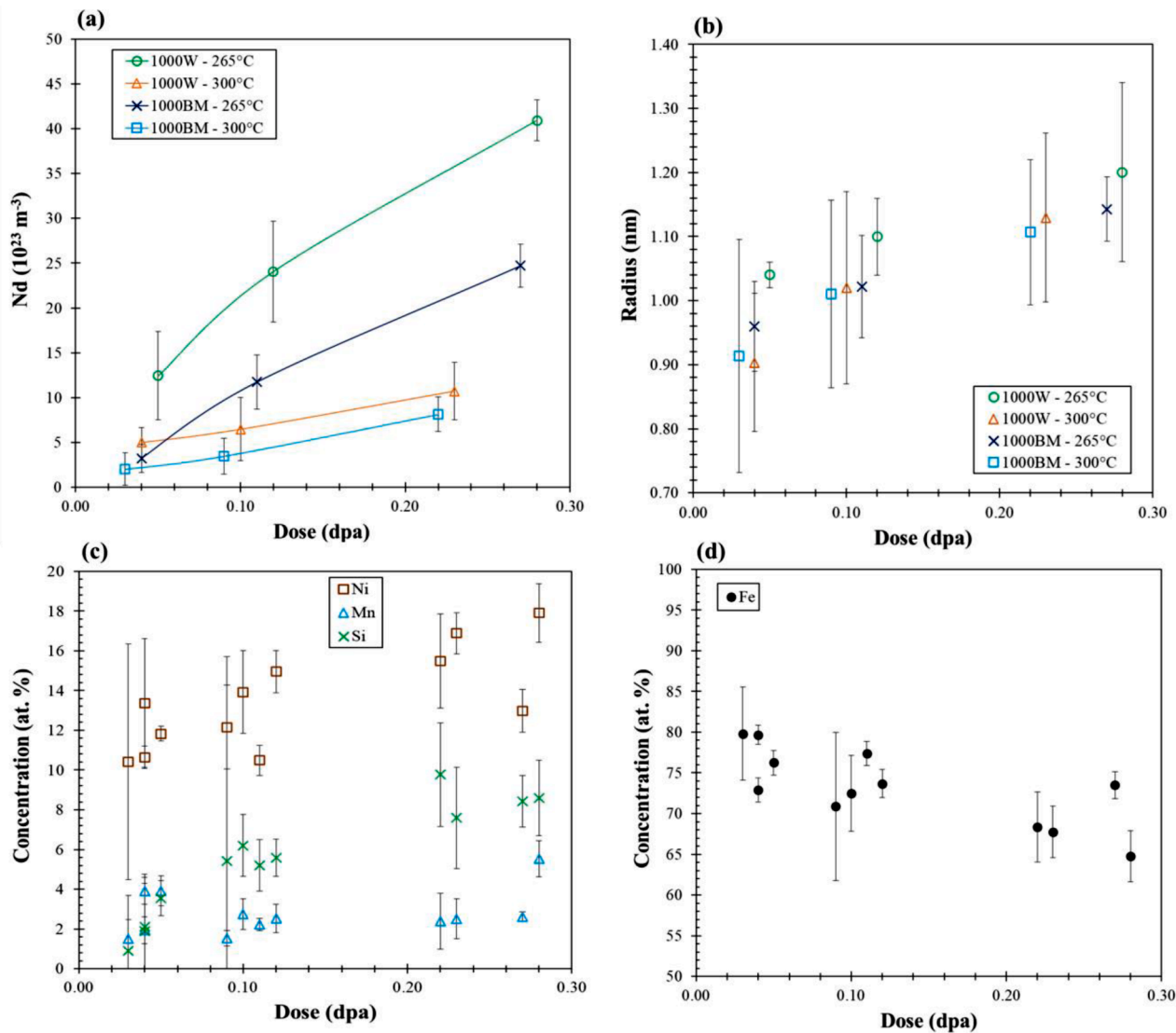


Fig. 10. Evolution of a) the number density (N_d) and b) the average radius (R) of solute clusters plotted as a function of the dose in dpa. c) and d) show respectively the evolution of solute and Fe levels in clusters as a function of the dose.

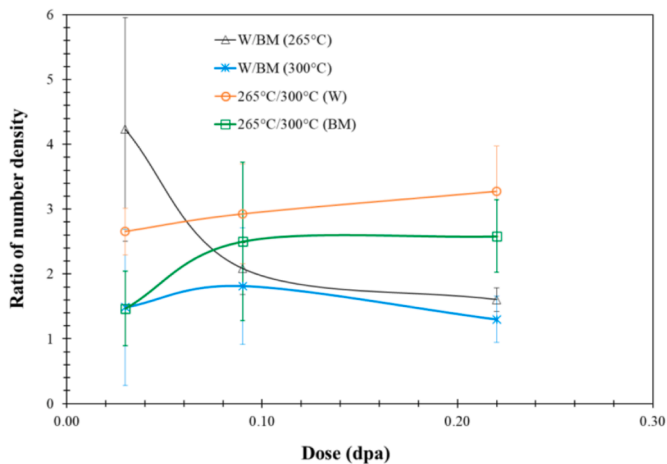


Fig. 11. Ratio of N_d . $N_d / N_{d,W} / N_{d,BM(265^\circ\text{C})}$ means the N_d of the 1000-W divided by the N_d of the 1000-BM at 265 °C. Black and blue curves show the contribution of the composition and green and orange curves represent the contribution of the irradiation temperature.

the bulk Ni concentration appears to have a large influence on the number density at low dose at 265 °C (black triangles). At high dose, the difference between the two parameters is significantly higher and reveals that irradiation temperature is the most impactful parameter in comparison to composition. About 1.5 times more clusters (blue and black curves) are formed in the material with the high Ni-content while between 2.6 and 3.3 times more clusters (green and orange curves) are formed when reducing the irradiation temperature from 300 to 265 °C.

Considering the observation on cluster composition and evolution with the neutron fluence, conclusion was made that flux coupling and radiation induced segregation mechanism take part in the cluster formation. In this case, solute clusters form around the defect sinks, the increase in N_d necessarily implies an increased number of these sinks. Thus, the effect of irradiation temperature on the density of defect sinks is higher than the effect of chemical composition. As already mentioned, immobilized small interstitial loops are efficient sinks where solute clusters can nucleate [41]. Hardouin Duparc et al. [42] have studied by transmission electron microscopy the density of dislocation loops at representative of low Cu RPV steels irradiated with electrons. They have shown that the higher the irradiation temperature, the lower the density of loops. This agrees with the irradiation temperature effect observed

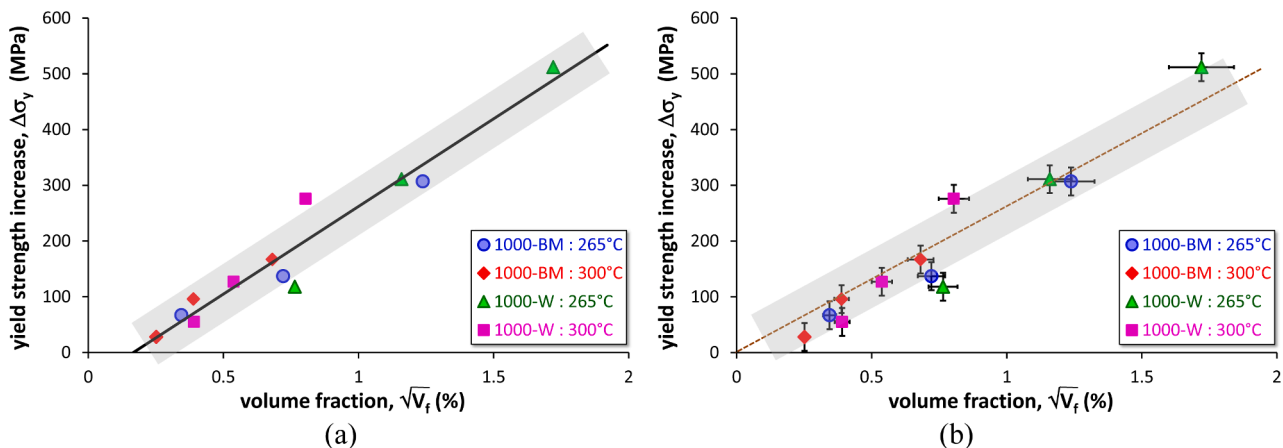


Fig. 12. Yield strength increase as a function of the $\sqrt{V_f}$ for all materials and conditions: best linear fit exhibiting an offset fluence (a) or linear fit intersecting the zero-origin (b). The volume fractions are in%.

here on the density of solute clusters and the proposed mechanism. It should be noticed, that in the case of a thermodynamic driving force, a lower temperature should also result in higher number density. Contribution of thermodynamic driving force, in addition to flux coupling cannot be completely excluded, in particular for the weld metal (high nickel), at the lower temperature. It could explain the high W/BM N_d ratio observed at the low fluence at 265 °C.

4.4. Hardening trend curve

Fig. 12 shows the relationship between the yield strength increase ($\Delta\sigma_y$) and the volume fraction of irradiation defects (V_f in%) as previously reported in other works [1,17]. The material hardening increases linearly with the square root of the volume fraction of defects ($\sqrt{V_f}$). As demonstrated by Bergner et al. [43], at low neutron doses, most of the irradiation-induced hardening or embrittlement is due to the formation of solute clusters.

Note that the trend line in **Fig. 12(a)** does not intersect the zero-origin. This could be due to a minimal amount of clustering that would be required to have an impact on the dislocation motion and, consequently, on the yield strength. Alternatively, the proportionality between $\Delta\sigma_y$ and $\sqrt{V_f}$ can still be argued given the statistical uncertainties related to the data points (see **Fig. 12(b)**).

5. Conclusions

Two VVER materials with Ni-content of 1.2% and 1.7%, respectively were investigated after neutron irradiation to three levels of neutron fluence at two different irradiation temperatures, 265 and 300 °C.

From the APT analysis, several points emerge:

- The irradiation results in the formation of Mn, Ni and Si rich solute clusters and the segregation of the same elements at crystal defects (dislocation lines, grain boundaries, interfaces). These features contain a majority of Fe. The ratio between the concentration of Ni, Mn and Si in the feature are similar to the bulk ratio, not the ones expected in G or Γ_2 phases.
- Fluence effect: the solute cluster number density, and to a lesser extend, the cluster radius increase with the dose. The level of Fe in solute clusters decreases when the dose increases.
- The irradiation temperature mainly affects the number density of clusters which are more numerous at lower temperature. This effect is more pronounced in the high nickel weld steel.
- The nickel bulk content also tends to promote cluster number density, in particular at low fluence and low temperature, but this Ni effect is lower than the temperature one.

All these observations support the existence of a radiation induced segregation mechanism as a strong contributor of solute clustering. Even if an additional contribution of thermodynamic driving force cannot be completely excluded, in particular in the 1000-W (partly due to high Ni concentration) irradiated at 265 °C, the cluster are not thermodynamically stable phases and their composition is proportional to the one of the unirradiated matrix.

The APT observations were used to estimate the radiation hardening, based on a simple Orowan model. The yield strength increase is linearly correlated with the square root of the volume fraction of the solute clusters.

CRedit authorship contribution statement

C. Courilleau: Investigation, Writing – original draft. **B. Radiguet:** Validation, Investigation, Writing – review & editing, Supervision. **R. Chaouadi:** Resources, Investigation, Writing – review & editing, Supervision. **E. Stergar:** Writing – review & editing, Investigation. **A. Duplessi:** Visualization, Validation. **P. Pareige:** Writing – review & editing, Supervision.

Declaration of Competing Interest

The authors declare that they have no known competing financial interests or personal relationships that could have appeared to influence the work reported in this paper.

Data availability

The authors do not have permission to share data.

Acknowledgments

GENESIS is supported by the Région Haute-Normandie, the Métropole Rouen Normandie, the CNRS via LABEX EMC and the French National Research Agency as a part of the program “Investissements d’avenir” with the reference ANR-11-EQPX-002

The authors acknowledge the financial support of the SCK CEN Academy.

References

- [1] A. Wagner, A. Ulbricht, F. Bergner, E. Altstadt, Influence of the copper impurity level on the irradiation response of reactor pressure vessel steels investigated by SANS, Nucl. Instru. Methods Phys. Res. Sect. B Beam Interact. Mater. Atoms 280 (2012) 98–102, <https://doi.org/10.1016/j.nimb.2012.03.008>. Jun.

- [2] M. Lambrecht, et al., On the correlation between irradiation-induced microstructural features and the hardening of reactor pressure vessel steels, *J. Nucl. Mater.* 406 (1) (2010) 84–89, <https://doi.org/10.1016/j.jnucmat.2010.05.020>. Nov.
- [3] G. Monnet, Multiscale modeling of irradiation hardening: application to important nuclear materials, *J. Nucl. Mater.* 508 (2018) 609–627, <https://doi.org/10.1016/j.jnucmat.2018.06.020>. Sep.
- [4] G.S. Was, *Fundamentals of Radiation Materials Science*, Springer New York, New York, NY, 2017, <https://doi.org/10.1007/978-1-4939-3438-6>.
- [5] L. Messina, T. Schuler, M. Nastar, M.C. Marinica, Solute diffusion by self-interstitial defects and radiation-induced segregation in ferritic FeX (X=Cr, Cu, Mn, Ni, P, Si) dilute alloys, *Acta Mater.* (2020) 20.
- [6] G.R. Odette, G.E. Lucas, Recent progress in understanding reactor pressure vessel steel embrittlement, *Radiat. Effects Defects in Solids* 144 (1–4) (1998) 189–231, <https://doi.org/10.1080/10420159808229676>. Jun.
- [7] D.J. Sprouster, et al., Structural characterization of nanoscale intermetallic precipitates in highly neutron irradiated reactor pressure vessel steels, *Scr. Mater.* 113 (2016) 18–22, <https://doi.org/10.1016/j.scriptamat.2015.10.019>. Mar.
- [8] H. Ke, et al., Thermodynamic and kinetic modeling of Mn-Ni-Si precipitates in low-Cu reactor pressure vessel steels, *Acta Mater.* 138 (2017) 10–26, <https://doi.org/10.1016/j.actamat.2017.07.021>. Oct.
- [9] P.B. Wells, et al., Evolution of manganese–nickel–silicon-dominated phases in highly irradiated reactor pressure vessel steels, *Acta Mater.* 80 (2014) 205–219, <https://doi.org/10.1016/j.actamat.2014.07.040>. Nov.
- [10] G.R. Odette, B.D. Wirth, A computational microscopy study of nanostructural evolution in irradiated pressure vessel steels, *J. Nucl. Mater.* 251 (1997) 157–171, [https://doi.org/10.1016/S0022-3115\(97\)00267-5](https://doi.org/10.1016/S0022-3115(97)00267-5). Nov.
- [11] T. Takeuchi, et al., Effects of chemical composition and dose on microstructure evolution and hardening of neutron-irradiated reactor pressure vessel steels, *J. Nucl. Mater.* 402 (2–3) (2010) 93–101, <https://doi.org/10.1016/j.jnucmat.2010.04.008>. Jul.
- [12] M.K. Miller, M.A. Sokolov, R.K. Nanstad, K.F. Russell, APT characterization of high nickel RPV steels, *J. Nucl. Mater.* 351 (1–3) (2006) 187–196, <https://doi.org/10.1016/j.jnucmat.2006.02.013>. Jun.
- [13] E. Meslin, B. Radiguet, P. Pareige, A. Barbu, Kinetic of solute clustering in neutron irradiated ferritic model alloys and a French pressure vessel steel investigated by atom probe tomography, *J. Nucl. Mater.* 399 (2–3) (2010) 137–145, <https://doi.org/10.1016/j.jnucmat.2009.11.012>. Apr.
- [14] E. Meslin, B. Radiguet, M. Loyer-Prost, Radiation-induced precipitation in a ferritic model alloy: an experimental and theoretical study, *Acta Mater.* 61 (16) (2013) 6246–6254, <https://doi.org/10.1016/j.actamat.2013.07.008>. Sep.
- [15] L.T. Belkacemi, E. Meslin, B. Décamps, B. Radiguet, J. Henry, Radiation-induced bcc-fcc phase transformation in a Fe3%Ni alloy, *Acta Mater.* 161 (2018) 61–72, <https://doi.org/10.1016/j.actamat.2018.08.031>. Dec.
- [16] B.M. Jenkins, et al., The effect of composition variations on the response of steels subjected to high fluence neutron irradiation, *Materialia* 11 (2020), 100717, <https://doi.org/10.1016/j.mta.2020.100717>. Jun.
- [17] N. Almirall, et al., Precipitation and hardening in irradiated low alloy steels with a wide range of Ni and Mn compositions, *Acta Mater.* 179 (2019) 119–128, <https://doi.org/10.1016/j.actamat.2019.08.027>. Oct.
- [18] S.J. Zinkle, “1.03 - radiation-induced effects on microstructure, 2023” p. 34.
- [19] E.A. Kuleshova, et al., Mechanisms of radiation embrittlement of VVER-1000 RPV steel at irradiation temperatures of (50–400) °C, *J. Nucl. Mater.* 490 (2017) 247–259, <https://doi.org/10.1016/j.jnucmat.2017.04.035>. Jul.
- [20] IAEA-TECDOC-1441, *Effects of Nickel On Irradiation Embrittlement of Light Water Reactor Pressure Vessel Steels*, International Atomic Energy Agency, Vienna, 2005. June.
- [21] N. Castin, L. Malerba, R. Chaouadi, Prediction of radiation induced hardening of reactor pressure vessel steels using artificial neural networks, *J. Nucl. Mater.* 408 (1) (2011) 30–39, <https://doi.org/10.1016/j.jnucmat.2010.10.039>. Jan.
- [22] J. Mathew, et al., Reactor pressure vessel embrittlement: insights from neural network modelling, *J. Nucl. Mater.* 502 (2018) 311–322, <https://doi.org/10.1016/j.jnucmat.2018.02.027>. Apr.
- [23] M.K. Miller, et al., Evolution of the nanostructure of VVER-1000 RPV materials under neutron irradiation and post irradiation annealing, *J. Nucl. Mater.* 385 (3) (2009) 615–622, <https://doi.org/10.1016/j.jnucmat.2009.01.299>. Apr.
- [24] N. Soneida, *Irradiation Embrittlement of Reactor Pressure Vessels (RPVs) in Nuclear Power Plants*, Elsevier, 2014.
- [25] A. Ulbricht, et al., Effect of neutron flux on an irradiation-induced microstructure and hardening of reactor pressure vessel steels, *Metals* 12 (3) (2022), <https://doi.org/10.3390/met12030369> (Basel) Art. no. 3, Mar.
- [26] L. Yao, J.M. Cairney, C. Zhu, S.P. Ringer, Optimisation of specimen temperature and pulse fraction in atom probe microscopy experiments on a microalloyed steel, *Ultramicroscopy* 111 (6) (2011) 648–651, <https://doi.org/10.1016/j.ultramicro.2010.12.032>. May.
- [27] Y. Yamaguchi, J. Takahashi, K. Kawakami, The study of quantitative analysis in atom probe analysis of alloying elements in steel, *Ultramicroscopy* 109 (5) (2009) 541–544, <https://doi.org/10.1016/j.ultramicro.2008.11.017>. Apr.
- [28] W. Lefebvre, F. Vurpillot, X. Sauvage, *Atom Probe Tomography - Put Theory Into Practice*, Elsevier Academic Press, 2016.
- [29] J.M. Hyde, G. Sha, E.A. Marquis, A. Morley, K.B. Wilford, T.J. Williams, A comparison of the structure of solute clusters formed during thermal ageing and irradiation, *Ultramicroscopy* 111 (6) (2011) 664–671, <https://doi.org/10.1016/j.ultramicro.2010.12.030>. May.
- [30] P.D. Edmondson, C.M. Parish, R.K. Nanstad, Using complimentary microscopy methods to examine Ni-Mn-Si-precipitates in highly-irradiated reactor pressure vessel steels, *Acta Mater.* 134 (2017) 31–39, <https://doi.org/10.1016/j.actamat.2017.05.043>. Aug.
- [31] N. Almirall, et al., The mechanistic implications of the high temperature, long time thermal stability of nanoscale Mn-Ni-Si precipitates in irradiated reactor pressure vessel steels, *Scr. Mater.* 181 (2020) 134–139, <https://doi.org/10.1016/j.scriptamat.2020.02.027>. May.
- [32] M.K. Miller, M.G. Hetherington, Local magnification effects in the atom probe, *Surf. Sci.* 246 (1–3) (1991) 442–449, [https://doi.org/10.1016/0039-6028\(91\)90449-3](https://doi.org/10.1016/0039-6028(91)90449-3). Apr.
- [33] F. Vurpillot, A. Bostel, D. Blavette, Topography overlaps and local magnification in three-dimensional atom probe, *Appl. Phys. Lett.* 76 (21) (2000) 3127–3129, <https://doi.org/10.1063/1.126545>. May.
- [34] N. Cunningham, “Study of the structure, composition, and stability of Y-Ti-O nanoscale features in nano-structured ferritic alloys, 2023” p. 351.
- [35] D. Blavette, F. Vurpillot, P. Pareige, A. Menand, A model accounting for spatial overlaps in 3D atom-probe microscopy, *Ultramicroscopy* 89 (1) (2001) 145–153, [https://doi.org/10.1016/S0304-3991\(01\)00120-6](https://doi.org/10.1016/S0304-3991(01)00120-6). Oct.
- [36] C. Hatzoglou, B. Radiguet, F. Vurpillot, P. Pareige, A chemical composition correction model for nanoclusters observed by APT - application to ODS steel nanoparticles, *J. Nucl. Mater.* 505 (2018) 240–248, <https://doi.org/10.1016/j.jnucmat.2018.03.057>. Jul.
- [37] C. Hatzoglou, B. Radiguet, P. Pareige, Experimental artefacts occurring during atom probe tomography analysis of oxide nanoparticles in metallic matrix: quantification and correction, *J. Nucl. Mater.* 492 (2017) 279–291, <https://doi.org/10.1016/j.jnucmat.2017.05.008>. Aug.
- [38] C. Hatzoglou, et al., Quantification of APT physical limitations on chemical composition of precipitates in Fe–Cr alloys, *J. Nucl. Mater.* 522 (2019) 64–73, <https://doi.org/10.1016/j.jnucmat.2019.05.022>. Aug.
- [39] G. Bonny, D. Terentyev, E.E. Zhurkin, L. Malerba, Monte Carlo study of decorated dislocation loops in FeNiMnCu model alloys, *J. Nucl. Mater.* 452 (1–3) (2014) 486–492, <https://doi.org/10.1016/j.jnucmat.2014.05.051>. Sep.
- [40] E. Meslin, et al., Characterization of neutron-irradiated ferritic model alloys and a RPV steel from combined APT, SANS, TEM and PAS analyses, *J. Nucl. Mater.* 406 (1) (2010) 73–83, <https://doi.org/10.1016/j.jnucmat.2009.12.021>. Nov.
- [41] N. Castin, et al., The dominant mechanisms for the formation of solute-rich clusters in low-Cu steels under irradiation, *Mater. Today Energy* 17 (2020), 100472, <https://doi.org/10.1016/j.mtener.2020.100472>. Sep.
- [42] A. Hardouin Duparc, C. Moingeon, N. Smetniansky-de-Grande, A. Barbu, Microstructure modelling of ferritic alloys under high flux 1 MeV electron irradiations, *J. Nucl. Mater.* 302 (2) (2002) 143–155, [https://doi.org/10.1016/S0022-3115\(02\)00776-6](https://doi.org/10.1016/S0022-3115(02)00776-6). Apr.
- [43] F. Bergner, et al., Contributions of Cu-rich clusters, dislocation loops and nanovoids to the irradiation-induced hardening of Cu-bearing low-Ni reactor pressure vessel steels, *J. Nucl. Mater.* 461 (2015) 37–44, <https://doi.org/10.1016/j.jnucmat.2015.02.031>. Jun.